

Many-Body Effects and Optical Properties of Single- and Double Layer $\alpha\text{-}\mathcal{T}_3$ Lattices

Andrii Iurov^{1*}, Godfrey Gumbs^{2,3}, and Danhong Huang^{4,5}

¹*Department of Physics and Computer Science,
Medgar Evers College of City University of New York,
Brooklyn, NY 11225, USA*

²*Department of Physics and Astronomy,
Hunter College of the City University of New York,
695 Park Avenue, New York, New York 10065, USA*

³*Donostia International Physics Center (DIPC),
P de Manuel Lardizabal, 4,
20018 San Sebastian, Basque Country, Spain*

⁴*Air Force Research Laboratory,
Space Vehicles Directorate,
Kirtland Air Force Base, New Mexico 87117,
USA* ⁵*Center for High Technology Materials,
University of New Mexico, 1313 Goddard SE,
Albuquerque, New Mexico, 87106, USA*

(Dated: February 1, 2022)

An extensive analytical and numerical investigation has been carried out to examine the role played by many-body effects on various $\alpha\text{-}\mathcal{T}_3$ materials under an off-resonance optical dressing field. Additionally, we explore its dependence on the hopping parameter α as well as the electron-light coupling strength λ_0 . The obtained dressed states due to mutual interaction between Dirac electrons and incident light are shown to demonstrate rather different electronic and optical properties in comparison with those in the absence of incident light. Specifically, various collective transport and optical properties of these electron dressed states are discussed in detail and compared for both single- and double layer $\alpha\text{-}\mathcal{T}_3$ lattices. All of these novel properties are due to the presence of a middle flat band and the interband transitions between it and an upper conduction band. Also, coupled plasmon dispersions for interacting double layer $\alpha\text{-}\mathcal{T}_3$ lattices are calculated, revealing a lower acoustic-like plasmon branch with tunable group velocity determined by both the layer separation and Fermi energy of each layer. Finally, a many-body theory is presented within the random-phase approximation for calculating the optical absorbance of doped multi-layered $\alpha\text{-}\mathcal{T}_3$ lattices in a linearly-polarized light field. We anticipate that the discoveries reported here could impact the design of the next-generation nano-optical and nano-plasmonic devices.

I. INTRODUCTION

Recently, the $\alpha\text{-}\mathcal{T}_3$ lattice model¹⁻³ has become the object of considerable attention within the well-studied family of Dirac-cone materials. The quasiparticles of these structures have a relativistic energy spectrum^{4,5}. Although $\alpha\text{-}\mathcal{T}_3$ still acquires a backbone honeycomb lattice as their atomic structure, their properties are quite different from those of graphene due to the presence of an additional atom at the center of each hexagon, usually referred to as a “hub.” Physically, the hopping amplitude between this hub atom (C) and one of the two inequivalent “rim” atoms (A or B) at the corners of each hexagon is not the same as the that between any two neighboring rim atoms. Therefore, the ratio between the hub-rim and rim-rim hopping amplitudes is chosen as a structural parameter α or simply taken as a geometry phase $\phi = \tan^{-1} \alpha$. In the special case of $\alpha = 1$ or $\phi = \pi/4$, these two hopping amplitudes become equal to each other, corresponding to the so-called “dice lattice”. On the other hand, the opposite case with $\alpha = 0$ simply reduces to a completely detached hub atom plus an uncoupled hexagonal lattice like graphene.

For all nonzero values of α , the low-energy electronic states of the $\alpha\text{-}\mathcal{T}_3$ model can be determined from a 3×3 pseudospin-1 Dirac-Weyl Hamiltonian. This provides an extra middle flat band at the Dirac point in comparison with the Dirac-cone band structure of graphene. The flat band has proven to be stable against various types of disorder and in the presence of various boundary conditions for $\alpha\text{-}\mathcal{T}_3$ -lattice nanoribbons^{6,7}. Importantly, a Berry curvature can be introduced by the structural parameter $\alpha \neq 1$ within the momentum space for conduction electrons in the $\alpha\text{-}\mathcal{T}_3$ model, leading to an anomalous thermal-equilibrium Hall current⁸ in addition to a thermal-equilibrium longitudinal current.

* E-mail contact: aiurov@mec.cuny.edu, theorist.physics@gmail.com

From a materials science perspective, lattices with a flat band could be fabricated based on a variety of naturally existing materials, such as tri-layers of $SrTiO_3/SrIrO_3/SrTiO_3$ ³. The flat-band included low-energy band structures were also realized in $Hg_{1-x}Cd_xTe$ quantum wells with an effective value of $\alpha = 1/\sqrt{3} \sim 0.577$ by implanting a specific doping level⁹. Additionally, artificial materials with flat energy bands were also constructed based on periodic electronic networks, spin systems under a critical magnetic-field strength¹⁰, Kagome structures¹¹, Lieb lattices embedded within a specific substrate¹² and optical lattices using interferometry of laser beams. For more inclusive references, we would refer readers to a recently published comprehensive review article about fabrication of artificial flat band materials¹³.

From the perspective of fundamental physics, all crucial properties of $\alpha\mathcal{T}_3$, such as, single-electronic^{8,14}, optical^{15–17}, magnetic^{18–21} and collective properties^{9,22,23} are greatly modified by the presence of the flat band, and therefore become strongly α dependent. Here, the largest modification is found in the vicinity of $\alpha = 0$ ^{24,25}. Moreover, from a technology and practical perspective, the so-called “*Floquet engineering*”, or control of the electronic dressed states through tuning light-electron interaction, both in two-dimensional lattices^{26–28} and on the surfaces of three-dimensional bulk materials^{29–31}, became a major interlayer between quantum optics and low-dimensional condensed matter physics over recent years due to advances in laser technologies.

We find that modification of single-electron states depends on the polarization of the incoming radiation. Circularly polarized light leads to opening a band gap of a few meV ^{27,32} and therefore a drop in the dc conductivity^{33–35} as well as electron tunneling^{36–39}. However, a linearly-polarized dressing field induces anisotropy³³ in both electron states and their dispersion, including modification of existing anisotropy in phosphorenes^{40,41}. Meanwhile, there might also exist a Lifshitz transition in bilayer graphene⁴².

For longitudinal plasmon excitations⁴³, there are active research investigations related to innovative two-dimensional lattices, including graphene^{44,45}, gapped graphene⁴⁶, silicene^{47,48}, transition metal dichalcogenides⁴⁹ and dice lattices⁹. The reason behind why plasmons in these materials appeal to us is their very wide frequency coverage up to the terahertz limit within the Coulomb-coupled system comprising a two-dimensional layer and a semi-infinite conductor, or the so-called *open systems*⁵⁰. Specifically, a fair amount of work has been done on the finite-temperature behavior of plasmons^{51–60}, their damping⁶¹, and plasmon-polaritons⁶² since each of these properties could be varied independently with temperature, and then the undamped plasmon branch could extend over an even higher energy range.

If the proposed modification to the single-electron states in $\alpha\mathcal{T}_3$ lattices can be achieved by means of “*Floquet engineering*”, there will be considerable interests in the control of either optical (e.g., plasmons) or transport (e.g., spin and valley-dependent currents) properties⁶³ for irradiated $\alpha\mathcal{T}_3$ materials. Here, the calculation of the polarization function, which describes the collective response and screening of an external potential by interacting electrons in a solid, becomes a key step. In fact, the optical properties, including plasmon modes and optical absorption, as well as the transport properties, covering scattering rates of conduction electrons by impurities and lattice phonons, can be deduced from this calculated polarization function depending on both frequency and wave vector. Analytic expressions for the polarization function in various frequency and wave vector regimes are found to be crucial and the most challenging part in each of the plasmon research mentioned above. Similar studies were carried out for finite-size fullerenes^{64,65}.

The outline of the rest of this paper is as follows. In Sec. II, we briefly review the single-electron states of $\alpha\mathcal{T}_3$ lattices and their energy dispersion with an emphasis on the new states corresponding to the middle flat band at the Dirac point. This also serves to establish the notation we used subsequently. Following this, in Sec. III, we discuss various properties of electron dressed states for the most general elliptically polarized incident light, as employed in Ref.¹⁷, including the limiting case with circularly-polarized and off-resonance dressing field in detail. The theory and calculation of the polarization function, plasmon dispersion and wave function overlap are presented in Sec. IV for a pseudospin-1 Hamiltonian. We also present and discuss the dependence on the structural parameter α in our calculated optical conductivity, coupled plasmon modes in double layer $\alpha\mathcal{T}_3$ lattices as well as the optical absorbance in Secs. V–VII, correspondingly. Finally, conclusions of this paper are drawn in Sec. VIII along with some discussions and remarks.

II. $\alpha\mathcal{T}_3$ AND DICE LATTICE MODELS: BASIC ELECTRONIC PROPERTIES

The energy dispersions of electronic states of a pseudospin-1 $\alpha\mathcal{T}_3$ lattice next to the two inequivalent valley points K and K' are determined by a (3×3) low-energy Hamiltonian matrix which explicitly depends on the structural parameter α , or $\phi = \tan^{-1} \alpha$, and is given by^{8,16}

$$\mathbb{H}_0(\mathbf{k} | \tau, \phi) = \hbar v_F \begin{bmatrix} 0 & k_-^\tau \cos \phi & 0 \\ k_+^\tau \cos \phi & 0 & k_-^\tau \sin \phi \\ 0 & k_+^\tau \sin \phi & 0 \end{bmatrix}, \quad (1)$$

where $k_\pm^\tau = \tau k_x \pm i k_y$ with $\tau = \pm$ labeling two valleys and v_F denoting the Fermi velocity.

Two solutions for Eq. (1) are found as

$$\varepsilon_{\tau, \phi}^{\gamma=\pm 1}(\mathbf{k}) = \gamma \hbar v_F k \quad (2)$$

with $\gamma = -1$ ($\gamma = +1$) for the valance (conduction) band, while the rest one is

$$\varepsilon_{\tau, \phi}^{\gamma=0}(\mathbf{k}) = 0, \quad (3)$$

which turns into a flat band. Here, all three bands are independent of phase ϕ or α .

Moreover, the corresponding wave functions for the valance and conduction bands are obtained as

$$\Psi_{\tau, \phi}^{\gamma=\pm 1}(\mathbf{k}) = \frac{1}{\sqrt{2}} \begin{bmatrix} \tau \cos \phi \, \mathbf{e}^{-i\tau\theta_{\mathbf{k}}} \\ \gamma \\ \tau \sin \phi \, \mathbf{e}^{+i\tau\theta_{\mathbf{k}}} \end{bmatrix}, \quad (4)$$

where $\theta_k = \arctan(k_y/k_x)$, while that for the flat band becomes

$$\Psi_{\tau, \phi}^{\gamma=0}(\mathbf{k}) = \begin{bmatrix} \sin \phi \, \mathbf{e}^{-i\tau\theta_{\mathbf{k}}} \\ 0 \\ -\cos \phi \, \mathbf{e}^{+i\tau\theta_{\mathbf{k}}} \end{bmatrix}. \quad (5)$$

As a special case, for a dice lattice with $\phi = \pi/4$, the Hamiltonian matrix in Eq. (1) reduces to⁹

$$\mathbb{H}_\tau^D(\mathbf{k}) = \frac{\hbar v_F}{\sqrt{2}} \begin{bmatrix} 0 & k_-^\tau & 0 \\ k_+^\tau & 0 & k_-^\tau \\ 0 & k_+^\tau & 0 \end{bmatrix}, \quad (6)$$

and the wave functions in Eqs. (4) and (5) become

$$\Psi_{\tau, D}^{\gamma=\pm 1}(\mathbf{k}) = \frac{1}{2} \begin{bmatrix} \tau \mathbf{e}^{-i\tau\theta_{\mathbf{k}}} \\ \sqrt{2} \gamma \\ \tau \mathbf{e}^{+i\tau\theta_{\mathbf{k}}} \end{bmatrix}, \quad (7)$$

and

$$\Psi_{\tau, D}^{\gamma=0}(\mathbf{k}) = \frac{1}{\sqrt{2}} \begin{bmatrix} \mathbf{e}^{-i\tau\theta_{\mathbf{k}}} \\ 0 \\ -\mathbf{e}^{+i\tau\theta_{\mathbf{k}}} \end{bmatrix}. \quad (8)$$

Different from Eqs. (7) and (8), the components of wave functions in Eqs. (4) and (5) for general α - \mathcal{T}_3 lattice clearly depend on phase ϕ . Therefore, we know the resulting overlap of wave functions as well as other quantum-mechanical observables will also rely on ϕ .

III. ELECTRON DRESSED STATES: CIRCULARLY-POLARIZED LIGHT

In this section, we focus on the derivation and discussing properties of the so-called *electron-photon dressed states*, which appear due to strong interaction of an Dirac electron in α - \mathcal{T}_3 lattice with an external off-resonant dressing field having a frequency much higher than the characteristic energies of our system.^{26,33} Specifically, we consider a light field in the form

$$\mathbf{A}^{(E)}(t) = \begin{Bmatrix} A_x^{(E)}(t) \\ A_y^{(E)}(t) \end{Bmatrix} = \frac{\mathcal{E}_0}{\omega} \begin{Bmatrix} \cos(\omega t) \\ \beta \sin(\omega t) \end{Bmatrix}, \quad (9)$$

where $\beta = \sin \Theta_e$ represents the ratio between field amplitudes along two axes of a polarization ellipse. In particular, the circularly polarized light corresponds to a limiting case with $\beta = 1$.

In the presence of incident light, the new Hamiltonian can be obtained by a canonical substitution for the wave vector \mathbf{k} through

$$k_{x,y} \implies k_{x,y} - \frac{e}{\hbar} A_{x,y}^{(E)}(t). \quad (10)$$

Consequently, Hamiltonian in Eq. (1) will acquire an additional *interaction* term $\mathbb{H}_I^{(e)}(t|\tau, \phi)$ and becomes

$$\mathbb{H}_0(\mathbf{k}|\tau, \phi) \implies \mathcal{H}(\mathbf{k}, t|\tau, \phi) = \mathbb{H}_0(\mathbf{k}|\tau, \phi) + \mathbb{H}_I^{(e)}(t|\tau, \phi). \quad (11)$$

Here, the second term of the new Hamiltonian in Eq. (11) is calculated explicitly as⁷⁴

$$\begin{aligned} \mathbb{H}_I^{(e)}(t|\tau, \phi) &= -\tau c_0 \sqrt{\cos^2(\omega t) + [\beta \sin(\omega t)]^2} \\ &\times \begin{bmatrix} 0 & \exp[-i\tau \Omega^\beta(t)] \cos \phi & 0 \\ \exp[+i\tau \Omega^\beta(t)] \cos \phi & 0 & \exp[-i\tau \Omega^\beta(t)] \sin \phi \\ 0 & \exp[i\tau \Omega^\beta(t)] \sin \phi & 0 \end{bmatrix}, \end{aligned} \quad (12)$$

where $c_0 = e\mathcal{E}_0 v_F / \omega$ quantify the strength of electron-light interaction (with the unit of energy). Moreover, we have introduced in Eq. (12) the notation $\Omega^\beta(t) = \tan^{-1} \{\beta \tan(\omega t)\}$. Equation (12) can be greatly simplified for a dice lattice with $\phi = \pi/4$. For all our future calculations, we would like to limit the consideration with circularly-polarized light, i.e., taking $\beta = 1$.

The energy eigenvalue for the flat band remains to be zero, while the dispersions of the valence and conduction bands are modified as

$$\varepsilon_\gamma(k, \lambda_0) = \gamma \sqrt{(\lambda_0 c_0 / 2)^2 + [\hbar v_F k (1 - \lambda_0^2 / 4)]^2}, \quad (13)$$

where $\lambda_0 = c_0 / \hbar \omega$ represents the dimensionless electron-light coupling parameter, and $\gamma = \pm 1$ for electrons (+) and holes (-). From Eq. (13), we know $\varepsilon_\gamma(k, \lambda_0)$ is independent of ϕ although its corresponding wave function could. For a finite wave vector $\mathbf{k} = \{k_x, k_y\}$ and a small electron-photon coupling constant $\lambda_0 \ll 1$, Eq. (13) can be further approximated as

$$\begin{aligned} \varepsilon_\gamma(k, \lambda_0) / \gamma &= \hbar v_F k - \left\{ \frac{1}{4} \hbar v_F k - \frac{1}{8} \frac{c_0^2}{\hbar v_F k} \right\} \lambda_0^2 \\ &+ c_0^2 \left\{ \frac{1}{32} \frac{1}{\hbar v_F k} - \frac{1}{128} \frac{c_0^2}{(\hbar v_F k)^3} \right\} \lambda_0^4 + \dots \end{aligned} \quad (14)$$

For dice lattice with $\phi = \pi/4$, its wave function is obtained from diagonalizing the eigenvalue equation of Hamiltonian in Eq. (11) as

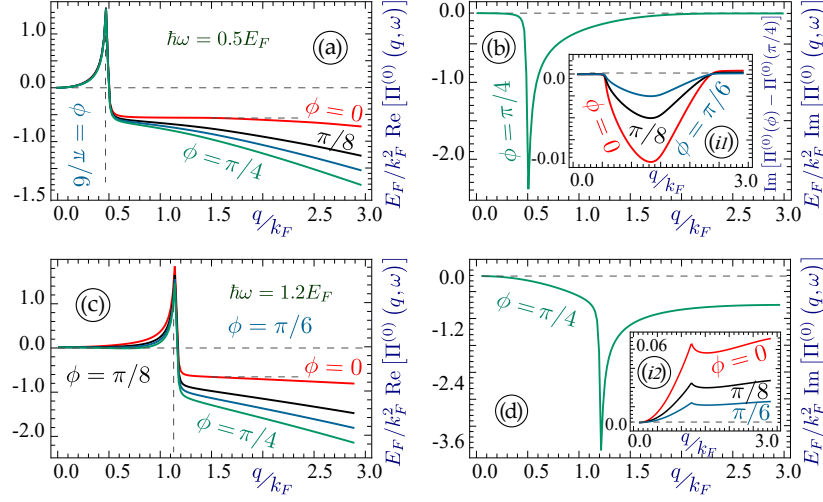


FIG. 1: (Color online) Polarization function $\Pi^{(0)}(q, \omega | \phi)$ in the units of k_F^2/E_F , calculated from Eq. (20), for $\lambda_0 = 0$ and various $\alpha\text{-}\mathcal{T}_3$ lattices as a function of scaled wave vector q/k_F (Fermi wave vector k_F). Two left panels describe the real part of $\Pi^{(0)}(q, \omega | \phi)$, while the right ones are for its imaginary part. The upper panels (a) and (b) correspond to a fixed frequency $\omega = 0.5 E_F/\hbar$, while the lower panels (c) and (d) show the results for $\omega = 1.2 E_F/\hbar$. For all plots, different color curves (red, black, blue and green) are associated with various values of ϕ (0, $\pi/8$, $\pi/6$ and $\pi/4$), respectively. Insets (i1) and (i2) demonstrate q dependence of the difference between the imaginary part of polarization functions of $\alpha\text{-}\mathcal{T}_3$ and dice lattice, i.e., $\text{Im} [\Pi^{(0)}(q, \omega | \phi)] - \text{Im} [\Pi^{(0)}(q, \omega | \pi/4)]$.

$$\Psi_\gamma^\tau(\mathbf{k}, \lambda_0) = \frac{1}{\sqrt{\mathcal{N}_\gamma^\tau}} \begin{bmatrix} \tau \mathcal{A}_{1,\gamma}^\tau e^{-i\tau\theta_\mathbf{k}} \\ \mathcal{A}_{2,\gamma}^\tau \\ \tau (\hbar v_F k)^2 e^{+i\tau\theta_\mathbf{k}} \end{bmatrix}, \quad (15)$$

where

$$\begin{aligned} \mathcal{A}_{1,\gamma}^\tau(k, \lambda_0) &= (\hbar v_F k)^2 + 2 \left(\delta_\lambda^2 - \gamma \tau \delta_\lambda \sqrt{(\hbar v_F k)^2 + \delta_\lambda^2} \right), \\ \mathcal{A}_{2,\gamma}^\tau(k, \lambda_0) &= \sqrt{2} \gamma (\hbar v_F k) \left(\sqrt{(\hbar v_F k)^2 + \delta_\lambda^2} - \gamma \tau \delta_\lambda \right), \\ \mathcal{N}_\gamma^\tau(k, \lambda_0 \ll 1) &\simeq 4 (\hbar v_F k)^4 - 4 \gamma \tau c_0 \lambda_0 (\hbar v_F k)^3 + 3 [c_0 \lambda_0 (\hbar v_F k)]^2 + \dots \end{aligned} \quad (16)$$

Here, the new parameter $\delta_\lambda = 2\lambda_0 c_0 / (4 - \lambda_0^2)$ is related but not exactly equal to the dressed-state energy gap $E_G \equiv 2\Delta_0 = \lambda_0 c_0$.

For a non-resonant field, λ_0 is expected to be small, and then, the amplitudes $\mathcal{A}_{1,\gamma}^\tau(k, \lambda_0)$ and $\mathcal{A}_{2,\gamma}^\tau(k, \lambda_0)$ in Eq. (16) could be expanded as

$$\begin{aligned} \mathcal{A}_{1,\gamma}^\tau(k, \lambda_0) &\approx (\hbar v_F k)^2 - \gamma \tau c_0 (\hbar v_F k) \lambda_0 + \frac{1}{2} c_0^2 \lambda_0^2 + \dots, \\ \mathcal{A}_{2,\gamma}^\tau(k, \lambda_0) &= \sqrt{2} \gamma (\hbar v_F k) \left(\sqrt{(\hbar v_F k)^2 + \delta_\lambda^2} - \gamma \tau \delta_\lambda \right). \end{aligned} \quad (17)$$

Therefore, the dressed-state wave function in Eq. (15) for the flat band can be approximated as

$$\Psi_0^\tau(\mathbf{k}, \lambda_0) = \frac{1}{\sqrt{\mathcal{N}_{\gamma=0}^\tau}} \begin{bmatrix} \hbar v_F k e^{-i\tau\theta_\mathbf{k}} \\ 2\sqrt{2} c_0 \lambda_0 / (4 - \lambda_0^2) \\ -\hbar v_F k e^{+i\tau\theta_\mathbf{k}} \end{bmatrix}, \quad (18)$$

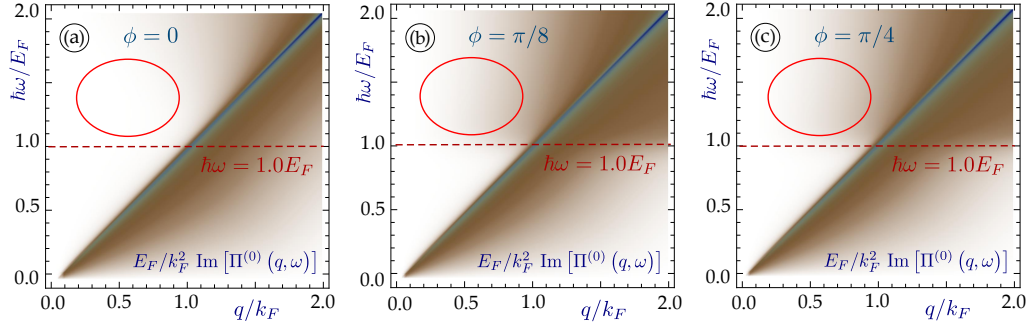


FIG. 2: (Color online) Density plots of $\text{Im}[\Pi^{(0)}(q, \omega | \phi)] \neq 0$ in the units of k_F^2/E_F for $\lambda_0 = 0$ and various $\alpha\text{-}\mathcal{T}_3$ lattices. Each panel corresponds to a different value of structural parameter α or phase ϕ : $\phi = 0$ (graphene) in (a), $\phi = \pi/8$ in (b), and $\phi = \pi/4$ (dice lattice) in (c).

where

$$\mathcal{N}_{\gamma=0}^{\tau}(k, \lambda_0 \ll 1) \simeq 2(\hbar v_F k)^2 + \frac{1}{2}(\lambda_0 c_0)^2 + \dots \quad (19)$$

Compared with Eq.(8), we find that once the irradiation is applied, the first and last components of wave function are no longer equal to each other (except for a phase difference) while the middle one becomes finite $\sim \lambda_0^2$, as expected from a finite energy gap^{17,33}.

IV. PLASMONS AND COLLECTIVE PROPERTIES

Most of the many-body electronic properties of a solid can be obtained from the calculated polarization function $\Pi^{(0)}(q, \omega | \phi, \lambda_0)$ at low temperatures with Fermi energy $E_F = \hbar v_F k_F$ with Fermi wave vector k_F , which represent a collective response of a system of many Coulomb-interacting electrons to an external potential. For an $\alpha\text{-}\mathcal{T}_3$ lattice, $\Pi^{(0)}(q, \omega | \phi, \lambda_0)$ takes the form

$$\begin{aligned} \Pi^{(0)}(q, \omega | \phi, \lambda_0) &= \frac{1}{\pi^2} \int d^2 \mathbf{k} \sum_{\gamma, \gamma'=0, \pm 1} \mathbb{O}_{\gamma, \gamma'}^{\tau}(\mathbf{k}, \mathbf{k} + \mathbf{q} | \phi, \lambda_0) \\ &\times \frac{\Theta[E_F - \varepsilon_{\gamma}(\mathbf{k}, \lambda_0)] - \Theta[E_F - \varepsilon_{\gamma'}(|\mathbf{k} + \mathbf{q}|, \lambda_0)]}{\hbar(\omega + i0^+) + \varepsilon_{\gamma}(\mathbf{k}, \lambda_0) - \varepsilon_{\gamma'}(|\mathbf{k} + \mathbf{q}|, \lambda_0)}, \end{aligned} \quad (20)$$

where $\varepsilon_{\gamma}(\mathbf{k}, \lambda_0)$ are the dressed-state energies given by Eq.(13), $\gamma = \pm 1$ corresponds to an electron or a hole state, and the Heaviside function $\Theta(x)$ is the limiting form of Fermi-Dirac distribution at zero temperature. The overlap function $\mathbb{O}_{\gamma, \gamma'}^{\tau}(\mathbf{k}, \mathbf{k} + \mathbf{q} | \phi, \lambda_0)$ introduced in Eq.(20) is simply a dot product of two wave functions $\Psi_{\tau, \phi}^{\gamma}(\mathbf{k}, \lambda_0)$ and $\Psi_{\tau, \phi}^{\gamma'}(\mathbf{k}', \lambda_0)$ with the wave vectors \mathbf{k} and $\mathbf{k}' = \mathbf{k} + \mathbf{q}$ as well as the band indices γ and γ' (also referred to the initial and scattered states)²⁴, i.e.,

$$\mathbb{O}_{\gamma, \gamma'}^{\tau}(\mathbf{k}, \mathbf{k} + \mathbf{q} | \phi, \lambda_0) = \left| \left\langle \Psi_{\tau, \phi}^{\gamma}(\mathbf{k}, \lambda_0) \left| \Psi_{\tau, \phi}^{\gamma'}(\mathbf{k} + \mathbf{q}, \lambda_0) \right. \right\rangle \right|^2, \quad (21)$$

where $k' = \sqrt{k^2 + q^2 + 2kq \cos \beta_{\mathbf{k}, \mathbf{k}'}}$ is the magnitude of vector \mathbf{k}' , and $\beta_{\mathbf{k}, \mathbf{k}'} = \theta_{\mathbf{k}'} - \theta_{\mathbf{k}}$ is the angle between \mathbf{k} and \mathbf{k}' .

The real part of $\Pi^{(0)}(q, \omega | \phi, \lambda_0)$ takes leading role in shaping the plasmon branches determined as the zeros of the dielectric function $\epsilon(q, \omega | \phi, \lambda_0)$ defined as

$$\epsilon(q, \omega | \phi, \lambda_0) = 1 - v(q) \Pi^{(0)}(q, \omega | \phi, \lambda_0), \quad (22)$$

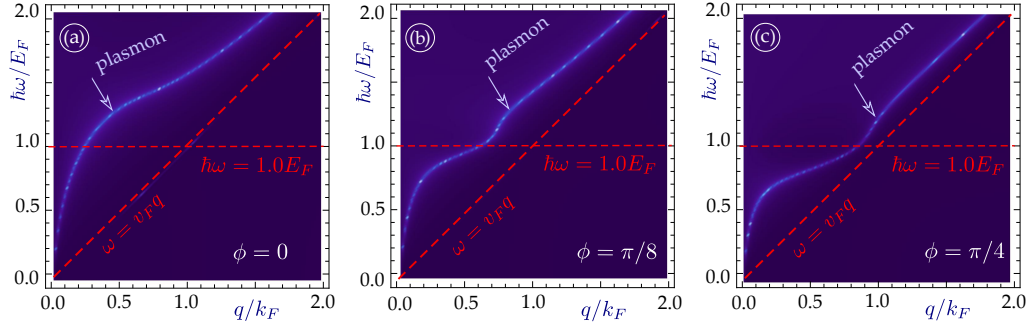


FIG. 3: (Color online) Density plots of $\Pi_{RPA}(q, \omega | \phi)$ presented in Eq. (23) in the units of k_F^2/E_F for $\lambda_0 = 0$ and various α - \mathcal{T}_3 lattices. Here, the plasmon dispersion (blue curve) is mapped out by the peak in $|\Pi_{RPA}(q, \omega | \phi)|$ as a function of ω for each given q . Three panels correspond to a different values of structural parameter α or phase ϕ : $\phi = 0$ (graphene) in (a), $\phi = \pi/8$ in (b), and $\phi = \pi/4$ (dice lattice) in (c).

where $v(q) = e^2/2\epsilon_0\epsilon_r q$ is the two-dimensional Coulomb potential with ϵ_r as the host-material dielectric constant. Alternatively, the regions of non-zero imaginary part of $\Pi^{(0)}(q, \omega | \phi, \lambda_0)$ specify the particle-hole excitation regions where plasmon modes are Landau damped and break into single-particle excitations. Therefore, we will concentrate only on the regions of the long-living plasmon modes with $\text{Im}[\Pi^{(0)}(q, \omega | \phi, \lambda_0)] = 0$. In the random-phase approximation²⁴ (RPA), the dielectric function in Eq. (22) can be employed to calculate Coulomb-renormalized polarization function $\Pi_{RPA}(q, \omega | \phi, \lambda_0)$, i.e.,

$$\Pi_{RPA}(q, \omega | \phi, \lambda_0) = \frac{\Pi^{(0)}(q, \omega | \phi, \lambda_0)}{\epsilon(q, \omega | \phi, \lambda_0)}, \quad (23)$$

where the plasmon dispersion, determined by $\text{Re}[\epsilon(q, \omega | \phi, \lambda_0)] = 0$, can be mapped out by the peak in the density plot of $\Pi_{RPA}(q, \omega | \phi, \lambda_0)$ as a function of ω for each given q .

As a first step, we focus on the polarization function $\Pi^{(0)}(q, \omega | \phi)$ for $\lambda_0 = 0$, plasmons and the energy loss function for non-irradiated α - \mathcal{T}_3 lattices with different values of α . Our numerical results for $\Pi^{(0)}(q, \omega | \phi)$ are presented in Fig. 1, where both real and imaginary parts of $\Pi^{(0)}(q, \omega | \phi)$ display a significant enhancement with increasing structural parameter α . As already mentioned, the most drastic variation of all optical properties occurs in the vicinity of $\alpha = 0$, while for the other limit of $\phi = \pi/4$ these changes are really small. As found from Fig. 1, the peaks of both real and imaginary parts of $\Pi^{(0)}(q, \omega | \phi)$, corresponding to the pole (denominator approaching zero) of Eq. (20), remain independent of α , which is expected for energy dispersions in Eq. (13). The difference between the imaginary parts of $\Pi^{(0)}(q, \omega | \phi)$ with two α values could be either negative or positive, as demonstrated in two insets of Fig. 1 for two peak values: $\omega = 0.5 E_F/\hbar$ in (i1) and $\omega = 1.2 E_F/\hbar$ in (i2).

Next, we look into the imaginary part of $\Pi^{(0)}(q, \omega | \phi)$ in Eq. (20) in order to identify the regions of the stable plasmons free from Landau damping $\text{Im}[\Pi^{(0)}(q, \omega | \phi)] \neq 0$, corresponding to the light (uncolored) areas within the ω - q plane in Fig. 2. We first notice that plasmons are not damped in the triangular region above the main diagonal $\omega = v_F q$ but below the Fermi energy $\omega = E_F/\hbar$ for all values of α . The area above the Fermi level acquires substantial plasmon damping for all non-zero α in contrast to that of graphene with $\alpha = 0$, where the particle-hole mode boundary is known as⁴⁴ $\omega = v_F(2k_F - q)$.

After the calculation of unscreened polarization function $\Pi^{(0)}(q, \omega | \phi)$ for $\lambda_0 = 0$, we are able to get the screened one $\Pi_{RPA}(q, \omega | \phi)$ from Eq. (23) based on the random-phase approximation, which is presented in Fig. 3. The shape of plasmon branches for all α - \mathcal{T}_3 lattices with $\alpha \neq 0$ in (b) and (c), i.e., having two separate “kinks” with a much smaller separation from the main diagonal $\omega = v_F q$, is very different from that of graphene plasmon demonstrated in (a) for $\alpha = 0$. Importantly, this separation becomes the smallest at the Fermi level with its specific values depending on the dielectric constant ϵ_r of the host material and structural parameter α . Especially, such a feature leads to a pinching of the plasmon branch in (c) for a dice lattice⁹. For all other intermediate values of α ($0 < \alpha < 1$), no pinching shows up as seen in (b). Instead, the plasmon branch reaches the closest separation from the diagonal line $\omega = v_F q$ as $\omega = E_F/\hbar$. On the other hand, in contrast to graphene, the plasmon branch for all nonzero finite α is free from Landau damping only limited to a small triangular region below the Fermi level while above the main diagonal simultaneously. This conclusion holds true even in the presence of circularly-polarized irradiation, as can be verified from Fig. 5 below.

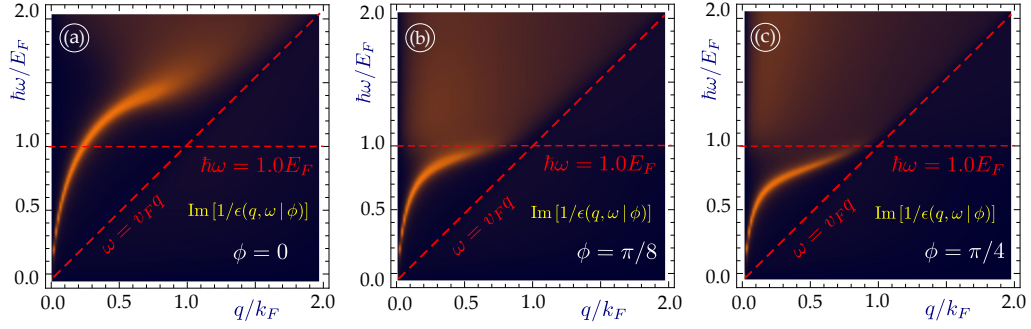


FIG. 4: (Color online) Density plots of energy loss function $\text{Im}[1/\epsilon(q, \omega | \phi)]$ given by Eq. (24) for $\lambda_0 = 0$ and various α - \mathcal{T}_3 lattices. Here, each panel corresponds to a different value of parameter α and phase ϕ : $\phi = 0$ (graphene) in (a), $\phi = \pi/8$ in (b), and $\phi = \pi/4$ (dice lattice) in (c).

In order to get a glimpse on kinetic-energy loss of incident charged particles, we would also calculate the electron energy-loss spectrum which is determined mainly by the imaginary part of the inverse dielectric function and given by

$$\begin{aligned} \mathcal{L}(q, \omega | \phi, \lambda_0) &= \text{Im} \left[\frac{1}{\epsilon(q, \omega | \phi, \lambda_0)} \right] \\ &= \frac{v(q) \text{Im} [\Pi^{(0)}(q, \omega | \phi, \lambda_0)]}{\{1 - v(q) \text{Re} [\Pi^{(0)}(q, \omega | \phi, \lambda_0)]\}^2 + \{v(q) \text{Im} [\Pi^{(0)}(q, \omega | \phi, \lambda_0)]\}^2}. \end{aligned} \quad (24)$$

The plots for numerical results on the loss function $\mathcal{L}(q, \omega | \phi)$ in Eq. (24) with $\lambda_0 = 0$ are presented in Fig. 4. The single bright orange curve features an undamped plasmon branch, while the extended region of brownish color is associated with various energy losses due to Landau damping to plasmon. From Figs. 4(b) and 4(c) for energy-loss function $\mathcal{L}(q, \omega | \phi)$, we once again demonstrate that all plasmon branches with nonzero α values will be strongly damped above the Fermi level. The physical nature of energy loss⁶⁶ has been revealed by Eq. (24) with its magnitude determined by the imaginary part of the polarization function while its dispersion by the first term of the denominator in Eq. (24).

Next, we turn to discussing the collective properties of an irradiated dice lattice with $\alpha = 1$. Figures 5, 6 and 7 display respectively, the numerical results for particle-hole modes, plasmon branches and energy loss functions for a dice lattice irradiated by circularly-polarized light with different light intensities c_0 and light-electron coupling strengths λ_0 , which provide a direct comparison with Figs. 2, 3 and 4 in the absence of a dressing field, i.e., taking $\lambda_0 = 0$.

From Fig. 5 we find that $\text{Im} [\Pi^{(0)}(q, \omega | \lambda_0)]$ for $\alpha = 1$ becomes zero only below the Fermi level and above the main diagonal $\omega = v_F q$. The boundary of particle-hole modes around the Fermi energy $\omega = E_F/\hbar$ does not acquire a noticeable dependence on λ_0 . The only visible difference due to dressing field is the “blue line”, or the negative peak in $\text{Im} [\Pi^{(0)}(q, \omega | \lambda_0)]$, shifts towards under the main diagonal, as found from Fig. 5(d). This behavior is related to light-induced modification to the energy dispersion in Eq. (13) which occurs in the denominator of Eq. (20). Physically, the change of a dressed-state energy arises from both light renormalization of the Fermi velocity and creation of an energy bandgap for nonzero α . Importantly, these two modifications are of the same order of magnitude $\sim \lambda_0$, which is quite different from graphene with $\alpha = 0$ where only the light-induced bandgap plays a role.²⁷ The pushing-down of the main diagonal in Fig. 5(d) can be attributed to the light renormalization of Fermi velocity in α - \mathcal{T}_3 lattice. This unique feature has a huge influence on suppressing the Landau damping of plasmons by decaying into particle-hole modes as shown in Fig. 6(d), where the brightness of blue curves (representing strength of plasmon modes) in Fig. 6 increases slightly with λ_0 in (a) and (b), followed by a dramatic decrease in (c), and ended with a huge increase again in (d).

The feature observed in Fig. 5 is also reflected in the energy loss function $\mathcal{L}(q, \omega | \lambda_0)$ given by Eq. (24) for $\alpha = 1$. While the undamped plasmon shows a small decrease of its frequency for $q/k_F < 1$ and $\hbar\omega/E_F < 1$ as seen in (a) - (c) of Fig. 7, the energy-loss curve or the undamped plasmon branch approaches the main diagonal for a larger $\lambda_0 = 0.3$ in (d). On the other hand, the damped plasmon branch for $q/k_F > 1$ tends to follow the blue line in Fig. 5 or the lines of the poles of both real and imaginary parts of $\Pi^{(0)}(q, \omega | \lambda_0)$ in Eq. (20). As λ_0 increases, both the blue line

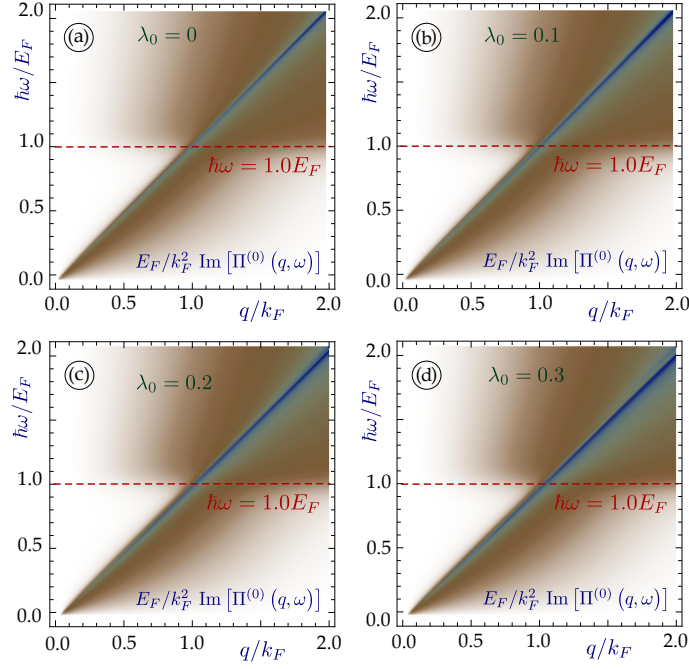


FIG. 5: (Color online) Density plots of $\text{Im} [\Pi^{(0)}(q, \omega | \lambda_0)] \neq 0$ in the units of k_F^2/E_F for an irradiated dice lattice with $\phi = \pi/4$. Each panel corresponds to a different light-electron coupling strength λ_0 of the imposed irradiation: $\lambda_0 = 0$ in (a), $\lambda_0 = 0.1$ in (b), $\lambda_0 = 0.2$ in (c), and $\lambda_0 = 0.3$ in (d).

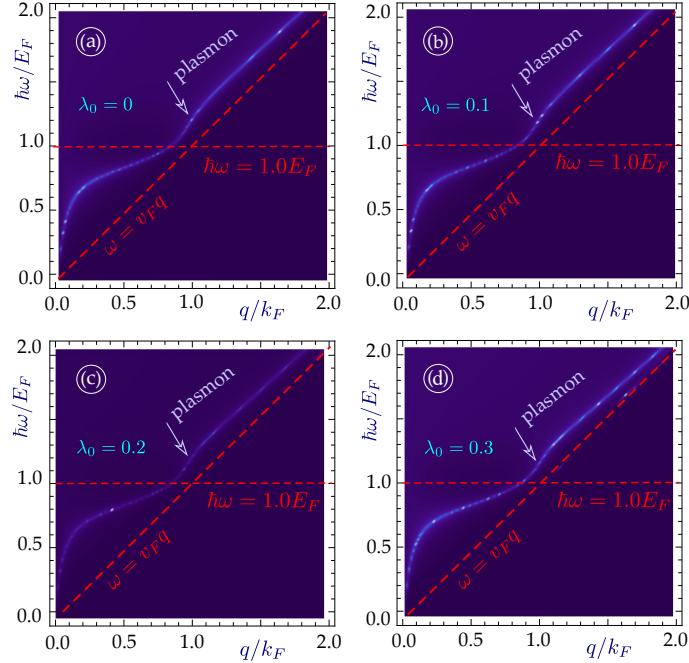


FIG. 6: (Color online) Density plots of $\Pi_{RPA}(q, \omega | \lambda_0)$ in the units of k_F^2/E_F for an irradiated dice lattice with $\phi = \pi/4$. Here, the plasmon dispersion (blue curve) is mapped out by the peak in correspond to the peak in $|\Pi_{RPA}(q, \omega | \lambda_0)|$ as a function of ω for each given q . Four panels correspond to different electron-light coupling strengths λ_0 of the imposed irradiation: $\lambda_0 = 0$ in (a), $\lambda_0 = 0.1$ in (b), $\lambda_0 = 0.2$ in (c), and $\lambda_0 = 0.3$ in (d).

and plasmon branch reduces their frequencies and becomes located below the main diagonal $\omega = v_F q$. The change of $\Pi^{(0)}(q, \omega | \lambda_0)$ and plasmon branch under the irradiation is quite conspicuous even though we limit our consideration to the small values of $\lambda_0 \ll 1$ for the off-resonant dressing field. The “kinky” shape of the plasmon branch is preserved and remains nearly the same in despite of the external irradiation.

V. OPTICAL CONDUCTIVITY IN α - \mathcal{T}_3 LATTICE

Optical conductivity connects the electric properties of a low-dimensional material, such as polarization current, with incident optical field. Therefore, we expect that optical conductivity will closely related to other optical properties of materials, such as absorption. Explicitly, the optical-current conductivity $\sigma_O(\omega | \phi, \lambda_0)$ can be calculated from the polarization function $\Pi^{(0)}(q, \omega | \phi, \lambda_0)$ in Eq. (20) under the long-wavelength limit,⁴⁸ yielding

$$\sigma_O(\omega | \phi, \lambda_0) = ie^2 \omega \lim_{q \rightarrow 0} \left[\frac{1}{q^2} \Pi^{(0)}(q, \omega | \phi, \lambda_0) \right]. \quad (25)$$

From Eq. (25), it is clear that the real part of $\sigma_O(\omega | \phi, \lambda_0)$ is associated with the imaginary part of $\Pi^{(0)}(q, \omega | \phi, \lambda_0)$ for single-particle excitation, while the imaginary part of $\sigma_O(\omega | \phi, \lambda_0)$ corresponds to the real part of $\Pi^{(0)}(q, \omega | \phi, \lambda_0)$ for induced optical polarization.

The calculated real part of $\sigma_O(\omega | \phi, \lambda_0)$ is presented Fig. 8(a), which describe the absorptive dissipation of polarization current or the damping of plasmon mode determined by the imaginary part of $\Pi^{(0)}(q, \omega | \phi, \lambda_0)$ in Eq. (20). From Fig. 8(a) we find the leading threshold step for the damping of plasmon excitation at $\omega = E_F/\hbar$ as $\alpha \neq 0$. For $\alpha = 0$, however, this leading threshold step shifts up to $\omega = 2E_F/\hbar$ for graphene. Additionally, numerical results for the imaginary part of $\sigma_O(\omega | \phi, \lambda_0)$ is displayed in Fig. 8(b), which leads to the dissipation of optical current due to the induced polarization field given by the real part of $\Pi^{(0)}(q, \omega | \phi, \lambda_0)$ or the plasmon excitation in our considered system. In a correspondence to the threshold steps for plasmon damping in Fig. 8(a), from Fig. 8(b) we find negative peaks at these frequencies related to starting of the undamped plasmon excitations. Interestingly, we also observe from Fig. 8(b) the secondary higher-frequency graphene-like negative peak even for $\phi \neq \pi/4$, which is associated with the appearance of the secondary higher-frequency threshold step in Fig. 8(a). Since the real and imaginary parts of $\Pi^{(0)}(q, \omega | \phi, \lambda_0)$ in Eq. (20) are related to each other by Krammers-Kronig relations, we should expect to see corresponding dependence between the two parts of $\sigma_O(\omega | \phi, \lambda_0)$, as shown in Figs. 8(a) and 8(b). Here, the strong negative peaks in (b) for $\text{Im}[\sigma_O(\omega | \phi, \lambda_0)]$ and the abrupt sudden jumps in (a) for $\text{Im}[\sigma_O(\omega | \phi, \lambda_0)]$ occur exactly at the same frequencies.

Physically, as seen from Fig. 8(a), we would like to point that the behavior for zero real part of $\sigma_O(\omega | \phi, \lambda_0)$ as a function of ω below a certain value is termed as Pauli-blocking effect.^{57,67} This threshold frequency depends primarily on the structural parameter α for different α - \mathcal{T}_3 lattices and originates from its limiting behavior of the imaginary part of $\Pi^{(0)}(q, \omega | \phi, \lambda_0)$ in Eq. (20) as $q \rightarrow 0$. For $0 < \alpha < 1$, this exists a two-step process, i.e., two sudden jumps in $\text{Re}[\sigma_O(\omega | \phi, \lambda_0)]$ at $\hbar\omega/E_F = 1, 2$. The first jump arises from the $0 \rightleftharpoons 1$ transitions of electrons from (and to) the flat band and can be represented by $\gamma = 0$ and $\gamma' = 1$ (or $\gamma = 1$ and $\gamma' = 0$) terms in their summations in Eq. (20). These transitions exist only in the presence of the flat band and disappear for graphene with $\alpha = 0$, in which only one jump occurs in $\text{Re}[\sigma_O(\omega | \phi, \lambda_0)]$ from the $-1 \rightleftharpoons +1$ transitions, or $\gamma = \pm 1$ and $\gamma' = \mp 1$, part of their summations in Eq. (20). Similarly, the boundary for particle-hole mode is found sitting at $\omega = 2E_F/\hbar - v_F q$ for graphene but at $E_F/\hbar - v_F q$ for all other non-zero α values.

VI. COUPLED PLASMONS IN α - \mathcal{T}_3 DOUBLE LAYERS

In this section, we investigate the properties of the dispersion relations of coupled plasmon modes in an interacting double layer α - \mathcal{T}_3 lattices in the absence of light irradiation. In this case, we expect that the individual plasmon modes in each of the two layers will be modified by the interlayer Coulomb interaction, and the whole system behaves in a way similar to two coupled quantum oscillators.

Plasmon excitations in two spatially separated and interacting layers with a two dimensional electron gas were investigated initially and reported in Ref.⁶⁸, and the coupled plasmon modes in an arbitrary number N of graphene layers interacting with a semi-infinite conductor were analyzed in Refs.⁵⁰ and⁶⁹. Generally, the total number of coupled-plasmon modes in such a system is equal to the number of conducting layers, i.e., $N + 1$ if the surface-plasmon mode in the semi-infinite conductor is also taken into consideration. For this case, each plasmon branch is

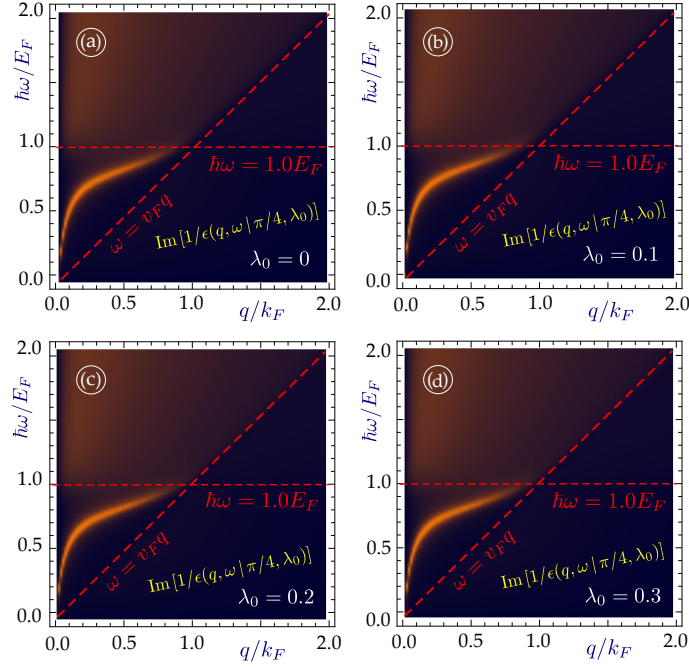


FIG. 7: (Color online) Density plots of energy loss function $\text{Im}[1/\epsilon(q, \omega | \lambda_0)]$ for an irradiated dice lattice with $\phi = \pi/4$. Here, each panel corresponds to a different electron-light coupling strength λ_0 : $\lambda_0 = 0$ in (a), $\lambda_0 = 0.1$ in (b), $\lambda_0 = 0.2$ in (c), and $\lambda_0 = 0.3$ in (d).

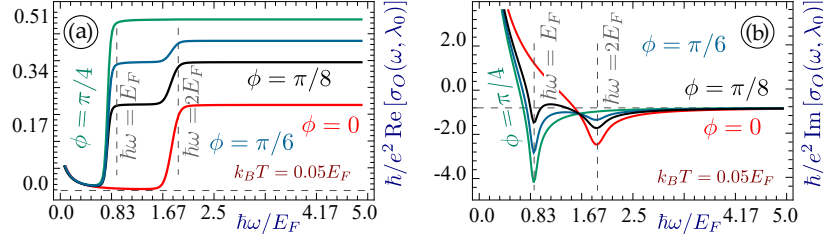


FIG. 8: (Color online) Optical conductivity $\sigma_O(\omega | \phi, \lambda_0)$ in the units of e^2/\hbar as a function of frequency ω at low temperature $k_B T/E_F = 0.05$. Panels (a) and (b) show the real and imaginary parts of $\sigma_O(\omega | \phi, \lambda_0)$, respectively. In both panels, each colored curve relates to a specific value of $\phi = \tan^{-1} \alpha$: red for $\phi = 0$ (graphene), black for $\phi = \pi/8$, blue for $\phi = \pi/6$, and green for $\phi = \pi/4$ (dice lattice).

often partially Landau damped at some critical frequency and wave vector. If only N two dimensional layers without a conducting surface are considered, the plasmon dispersions will be determined by a linear and homogeneous $(N \times N)$ matrix equation, where each individual equation is coupled to all other ones by the inter-layer potential as given by Eq. (27).

Specifically, for a double layer system composed of two Coulomb interacting $\alpha\text{-}\mathcal{T}_3$ lattices separated by a distance d from each other, the resulting determinant equation takes the form

$$\left\{1 - \mathbb{V}_0(q) \Pi^{(0)}(q, \omega | \phi_1)\right\} \left\{1 - \mathbb{V}_0(q) \Pi^{(0)}(q, \omega | \phi_2)\right\} - [\mathbb{V}_1(q)]^2 \Pi^{(0)}(q, \omega | \phi_1) \Pi^{(0)}(q, \omega | \phi_2) = 0, \quad (26)$$

where $\Pi^{(0)}(q, \omega | \phi_{1,2})$ represent the polarization functions of two layers labeled by $i = 1, 2$, and the intra-layer (0) and inter-layer (1) Coulomb potentials are found as

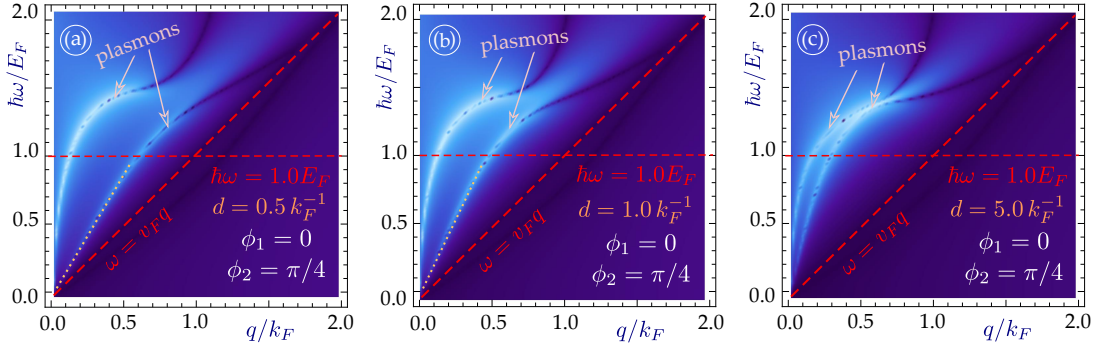


FIG. 9: (Color online) Density plots of plasmon dispersion relations calculated from Eq. (26) for two Coulomb-coupled dice lattice layers with $\phi_1 = 0$ and $\phi_2 = \pi/4$. Here, each panel corresponds to chosen layer separation: $d = 0.5 k_F^{-1}$ in (a), $d = 1.0 k_F^{-1}$ in (b), and $d = 5.0 k_F^{-1}$ in (c).

$$\begin{aligned} \mathbb{V}_0(q) &= \frac{e^2}{2\epsilon_0\epsilon_r q}, \\ \mathbb{V}_1(q) &= \frac{e^2}{2\epsilon_0\epsilon_r q} \exp(-qd). \end{aligned} \quad (27)$$

Here, we assume that the Fermi energies in both layers is equal to each other, i.e., $E_{F,1} = E_{F,2}$, and the two layers are otherwise identical except for having different phases $\phi_1 \neq \phi_2$ (or $\alpha_1 \neq \alpha_2$).

Our numerical results for coupled plasmon modes within two interacting layers of $\alpha\text{-}\mathcal{T}_3$ lattices are presented in Figs. 9 and 10. Two different layers are chosen in Fig. 9 with their phases $\phi_1 = 0$ and $\phi_2 = \pi/4$ for graphene and dice lattice, respectively, whereas the same dice lattice is chosen in both layers for Fig. 10. The presence of the inter-layer potential $\mathbb{V}_1(q)$ substantially modifies the dispersions of these two coupled plasmon modes with a splitting gap as the layer separation d is decreased, as it is evident in Fig. 9(a). In fact, the interlayer interaction plays a role only for separations up to $d \approx k_F^{-1}$. However, it is rapidly decreased once the layer separation is increased and reaches $d = 5.0 k_F^{-1}$. Then, the off-diagonal terms in Eq. (26) become negligibly small, as demonstrated in both Figs. 9(c) and 10(c).

The most crucial finding from Figs. 9 and 10 is that *the lower acoustic plasmon branch remains linear* despite the choice of the phase ϕ_i or separation d between two layers as long as the second term in Eq. (26) remains substantial. This result is similar to that found for graphene reported in Ref. ⁶⁸. On the contrary, the higher branch always displays a $\propto \sqrt{q}$ dependence and therefore reaches the regions for particle-hole excitations at smaller q values.

The plasmon damping is determined by the outermost boundary of the particle-hole modes which corresponds to a larger phase ϕ . Therefore, all plasmon branches are free from damping inside the triangle region determined by $\omega < E_F/\hbar$ and $\omega > v_F q$, as we discussed above. Additionally, when we compare Fig. 9 with Fig. 10, we find much stronger damping for the plasmon excitations above the line $\omega = E_F/\hbar$ in Fig. 10 as two layers are assumed to be the same with $\phi_1 = \phi_2$, and two plasmon branches merging together as q gets close to k_F . Technically, we can always achieve a lower slope for the linear plasmon branch by varying the separation d between the two layers. At the same time, a more pronounced change in the plasmon dispersion could also be achieved by varying the Fermi energy $E_{F,i}$ for one of the two layers, since the plasmon frequency is nearly proportional to the Fermi energy in the long-wavelength limit.

VII. OPTICAL ABSORPTION IN $\alpha\text{-}\mathcal{T}_3$ MULTI-LAYER SYSTEM

The degree of optical absorption, or the loss of photons, in a system can be quantified by the so-called dimensionless absorbance $\Gamma_{abs}(\omega)$,^{70,71} which is calculated as

$$\Gamma_{abs}(\omega) = \frac{\omega\sqrt{\epsilon_r}}{c} [1 + \rho_{ph}(\omega)] \text{Im}[\alpha(\omega)] , \quad (28)$$

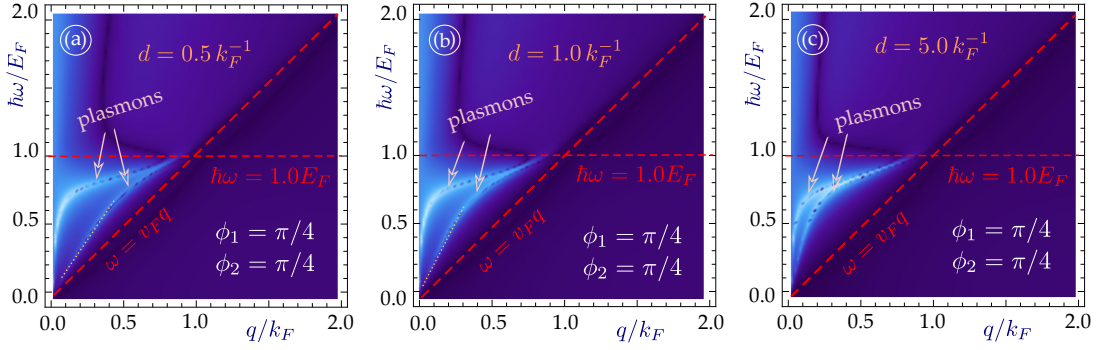


FIG. 10: (Color online) Density plots of plasmon dispersions based on Eq. (26) for two Coulomb-coupled layers composed of dice lattices with $\phi_1 = \phi_2 = \pi/4$. Here, each panel corresponds to the following separations between the two layers: $d = 0.5 k_F^{-1}$ in (a), $d = 1.0 k_F^{-1}$ in (b), and $d = 5.0 k_F^{-1}$ in (c).

where $\hbar\omega$ is the energy of incident photons. At low temperatures, i.e., $k_B T \ll \hbar\omega$, the photon occupation number $\rho_{ph}(\omega)$ becomes negligible due to

$$\rho_{ph}(\omega) = \left[\exp\left(\frac{\hbar\omega}{k_B T}\right) - 1 \right]^{-1} \sim \exp\left[-\frac{\hbar\omega}{k_B T}\right] \ll 1. \quad (29)$$

On the other hand, the Lorentz like factor (in units of length) introduced in Eq. (28) is calculated as⁷²

$$\alpha(\omega) = -\left(\frac{2e^2}{\epsilon_0 \epsilon_r}\right) \pi R_0^2 \sum_{j=1}^N \int \frac{d^2 \mathbf{q}}{(2\pi)^2} \exp\left\{-\frac{q^2 R_0^2}{4}\right\} \mathcal{Q}_j(q, \omega | \{\phi\}), \quad (30)$$

where the transverse linearly polarized light field is incident perpendicularly to layers with a beam radius R_0 . The optical response function $\mathcal{Q}_j(q, \omega | \{\phi\})$ in Eq. (30) for the j 's layer in an N -layer system has been modified for the Dirac cone dispersion from its original expression given in Ref.⁷³, leading to

$$\mathcal{Q}_j(q, \omega | \{\phi\}) = \chi_{j,j}(q, \omega | \{\phi\}) \left(\frac{v_F q}{k_F \omega}\right)^2, \quad (31)$$

where $\{\phi\}$ represents the full set $\{\phi_1, \phi_2, \dots, \phi_{N-1}, \phi_N\}$, v_F and $k_F = \sqrt{\pi n_0}$ are Fermi velocity and wave number of Dirac electrons, and only electron doping in the conduction band is assumed with an areal density n_0 . Moreover, $\chi_{j,j'}(q, \omega | \{\phi\})$ introduced in Eq. (31) can be calculated from the regular non-interacting polarization function $\Pi_j^{(0)}(q, \omega | \phi_j)$ in Eq. (20) for the j 's layer by taking into account the Coulomb coupling between various α - \mathcal{T}_3 layers. This yields

$$\begin{aligned} \chi_{j,j'}(q, \omega | \{\phi\}) &= \Pi_j^{(0)}(q, \omega | \phi_j) \delta_{j,j'} \\ &+ \Pi_j^{(0)}(q, \omega | \phi_j) \sum_{s(\neq j')=1}^N \mathbb{V}_{j,s}(q) \chi_{s,j'}(q, \omega | \{\phi\}), \end{aligned} \quad (32)$$

where $\mathbb{V}_{j,s}(q) = (e^2/2\epsilon_0 \epsilon_r q) \exp(-qd|s-j|)$ represents either interlayer ($j \neq s$) or intralayer ($j = s$) Coulomb interaction. Equation (32) is physically equivalent to the random-phase approximation for including the screening from both intra-layer and inter-layer Coulomb interactions in a multi-layer system. By solving Eq. (32) to determine $\chi_{j,j}(q, \omega | \{\phi\})$, and then employing Eqs. (30) and (31), we eventually arrive at a result for the absorbance $\Gamma_{abs}(\omega)$ in Eq. (28).

VIII. CONCLUDING REMARKS AND SUMMARY

We have investigated fundamental characteristics of the collective, transport and optical properties of electron dressed states in single and double layer α - \mathcal{T}_3 materials. These dressed electronic states, due to the interaction between

electrons and incident circularly polarized light field within the off-resonant regime, acquire new light renormalized energy dispersion. Additionally, this leads to modified Fermi velocity and opening an energy gap much smaller than that for irradiated graphene. It is also worthy of note that we have carefully analyzed the role played by many-body effects on plasmon excitations, and the way in which they are affected by the hopping parameter α as well as the electron-light coupling strength λ_0 for a dice lattice when $\alpha = 1$. The interplay between all these effects varies in scope and even compete with each other, resulting in a practical opportunity for light being used for tuning the electronic and collective properties of optical materials by means of Floquet engineering.

From the results of our calculations, we have discovered that all the unique properties of $\alpha\text{-}\mathcal{T}_3$ originate from the presence of a flat band in the energy dispersions and the resulting inter-band transitions. Specifically, we have focused our attention on the optical conductivity and demonstrated how the transitions between the flat and conduction bands give rise to a step-like increase in the optical conductivity at the Fermi energy not present in graphene.

We note our calculations of the coupled plasmon excitations for interacting double layer $\alpha\text{-}\mathcal{T}_3$ lattices. Their dispersions reveal that the lower plasmon branch remains linear (an acoustic mode) for all α . However, this group velocity is changed by varying the layer separation and doping level of individual layers. Such a novel feature provides us with an undamped plasmon excitation below the Fermi level for large wave vectors.

Finally, we have established a theoretical framework for computing the optical absorbance of doped multi-layered $\alpha\text{-}\mathcal{T}_3$ in the presence of linearly polarized light by including both inter-layer and intra-layer Coulomb interactions between Dirac electrons. All explored optical properties of these novel pseudospin-1 materials in this paper represent important and surprising discoveries, which could be applied in the construction of new optical and plasmonic nanoscale devices.

Acknowledgement(s)

G.G. would like to acknowledge the financial support from the Air Force Research Laboratory (AFRL) through grant FA9453-18-1-0100 and award FA2386-18-1-0120. D.H. thanks the supports from the Laboratory University Collaboration Initiative (LUCI) program and from the Air Force Office of Scientific Research (AFOSR).

Disclosure statement

No potential conflict of interest was reported by the authors.

-
- ¹ Moller, G., & Cooper, N. R. (2012). Correlated phases of bosons in the flat lowest band of the dice lattice. *Physical Review Letters*, **108**(4), 045306.
 - ² Illes, E. (2017). Properties of the $\alpha\text{-}\mathcal{T}_3$ Model (Doctoral Dissertation).
 - ³ Wang, F., & Ran, Y. (2011). Nearly flat band with Chern number $C = 2$ on the dice lattice. *Physical Review B*, **84**(24), 241103.
 - ⁴ Geim, A. K., & Novoselov, K. S. (2010). The rise of graphene. In *Nanoscience and technology: a collection of reviews from nature journals* (pp. 11-19).
 - ⁵ Neto, A. C., Guinea, F., Peres, N. M., Novoselov, K. S., & Geim, A. K. (2009). The electronic properties of graphene. *Reviews of Modern Physics*, **81**(1), 109.
 - ⁶ Oriekhov, D. O., Gorbar, E. V., & Gusynin, V. P. (2018). Electronic states of pseudospin-1 fermions in dice lattice ribbon. *Low Temperature Physics*, **44**(12), 1313-1324.
 - ⁷ Bugaiko, O. V., & Oriekhov, D. O. (2019). Electronic states of pseudospin-1 fermions in $\alpha\text{-}\mathcal{T}_3$ lattice ribbons in a magnetic field. *arXiv preprint arXiv:1902.02367*.
 - ⁸ Huang, D., Iurov, A., Xu, H. Y., Lai, Y. C., and Gumbs, G. (2019). Interplay of Lorentz-Berry forces in position-momentum spaces for valley-dependent impurity scattering in $\alpha\text{-}\mathcal{T}_3$ lattices. *Physical Review B*, **99**(24), 245412.
 - ⁹ Malcolm, J. D., & Nicol, E. J. (2016). Frequency-dependent polarizability, plasmons, and screening in the two-dimensional pseudospin-1 dice lattice. *Physical Review B*, **93**(16), 165433.
 - ¹⁰ Naud, C., Faini, G., & Maillly, D. (2001). Aharonov-Bohm cages in 2D normal metal networks. *Physical Review Letters*, **86**(22), 5104.
 - ¹¹ Ruostekoski, J. (2009). Optical kagome lattice for ultracold atoms with nearest neighbor interactions. *Physical Review Letters*, **103**(8), 080406.
 - ¹² Slot, M. R., Gardenier, T. S., Jacobse, P. H., van Miert, G. C., Kempkes, S. N., Zevenhuizen, S. J., & Swart, I. (2017). Experimental realization and characterization of an electronic Lieb lattice. *Nature Physics*, **13**(7), 672-676.

- ¹³ Leykam, D., Andreanov, A., & Flach, S. (2018). Artificial flat band systems: from lattice models to experiments. *Advances in Physics: X*, **3**(1), 1473052.
- ¹⁴ Gorbar, E. V., Gusynin, V. P., & Oriekhov, D. O. (2019). Electron states for gapped pseudospin-1 fermions in the field of a charged impurity. *Physical Review B*, **99**(15), 155124.
- ¹⁵ Chen, L., Zuber, J., Ma, Z., & Zhang, C. (2019). Nonlinear optical response of the α - T_3 model due to the nontrivial topology of the band dispersion. *Physical Review B*, **100**(3), 035440.
- ¹⁶ Dey, B., & Ghosh, T. K. (2018). Photoinduced valley and electron-hole symmetry breaking in α - T_3 lattice: The role of a variable Berry phase. *Physical Review B*, **98**(7), 075422.
- ¹⁷ Iurov, A., Gumbs, G., and Huang, D. (2019). Peculiar electronic states, symmetries, and Berry phases in irradiated α - T_3 materials. *Physical Review B*, **99**(20), 205135.
- ¹⁸ Raoux, A., Morigi, M., Fuchs, J. N., Piechon, F., and Montambaux, G. (2014). From dia- to paramagnetic orbital susceptibility of massless fermions. *Physical Review Letters*, **112**(2), 026402.
- ¹⁹ Illes, E., & Nicol, E. J. (2016). Magnetic properties of the α - T_3 model: Magneto-optical conductivity and the Hofstadter butterfly. *Physical Review B*, **94**(12), 125435.
- ²⁰ Biswas, T., & Ghosh, T. K. (2016). Magnetotransport properties of the α - T_3 model. *Journal of Physics: Condensed Matter*, **28**(49), 495302.
- ²¹ Biswas, T., & Ghosh, T. K. (2018). Dynamics of a quasiparticle in the α - T_3 model: role of pseudospin polarization and transverse magnetic field on zitterbewegung. *Journal of Physics: Condensed Matter*, **30**(7), 075301.
- ²² Dey, B., Kapri, P., Pal, O., & Ghosh, T. K. (2020). Unconventional phases in Haldane model of dice lattice. *arXiv preprint arXiv:2003.07143*.
- ²³ Oriekhov, D. O., & Gusynin, V. P. (2020). RKKY interaction in doped pseudospin-1 fermion system at finite temperature. *arXiv preprint arXiv:2001.00272*.
- ²⁴ Iurov, A., Zhemchuzhna, L., Dahal, D., Gumbs, G., and Huang, D. (2020). Quantum-statistical theory for laser-tuned transport and optical conductivities of dressed electrons in α - T_3 materials. *Physical Review B*, **101**(3), 035129.
- ²⁵ Mojarro, M. A., Ibarra-Sierra, V. G., Sandoval-Santana, J. C., Carrillo-Bastos, R., & Naumis, G. G. (2020). Electron transitions for Dirac Hamiltonians with flat-bands under electromagnetic radiation and its application to the α - T_3 graphene model. *arXiv preprint arXiv:2001.11661*.
- ²⁶ Kibis, O. V., Dini, K., Iorsh, I. V., and Shelykh, I. A. (2017). All-optical band engineering of gapped Dirac materials. *Physical Review B*, **95**(12), 125401.
- ²⁷ Kibis, O. V. (2010). Metal-insulator transition in graphene induced by circularly polarized photons. *Physical Review B*, **81**(16), 165433.
- ²⁸ Sandoval-Santana, J. C., Ibarra-Sierra, V. G., Kunold, A., & Naumis, G. G. (2020). Floquet spectrum for anisotropic and tilted Dirac materials under linearly polarized light at all field intensities. *arXiv preprint arXiv:2003.12119*.
- ²⁹ Daz-Fernandez, A., Díaz, E., Gómez-León, A., Platero, G., & Domínguez-Adame, F. (2019). Floquet engineering of Dirac cones on the surface of a topological insulator. *Physical Review B*, **100**(7), 075412.
- ³⁰ Kyriienko, O., Kibis, O. V., & Shelykh, I. A. (2019). Optically induced topological states on the surface of mercury telluride. *Physical Review B*, **99**(11), 115411.
- ³¹ Islam, S. F., & Zyuzin, A. A. (2019). Photoinduced interfacial chiral modes in threefold topological semimetal. *Physical Review B*, **100**(16), 165302.
- ³² Kibis, O. V. (2011). Dissipationless electron transport in photon-dressed nanostructures. *Physical Review Letters*, **107**(10), 106802.
- ³³ Kristinsson, K., Kibis, O. V., Morina, S., and Shelykh, I. A. (2016). Control of electronic transport in graphene by electromagnetic dressing. *Scientific Reports*, **6**, 20082.
- ³⁴ Iurov, A., Gumbs, G., and Huang, D. (2017). Exchange and correlation energies in silicene illuminated by circularly polarized light. *Journal of Modern Optics*, **64**(9), 913-920.
- ³⁵ Mandal, S., Dini, K., Kibis, O. V., and Liew, T. C. H. (2019). On the possibility of a terahertz light emitting diode based on a dressed quantum well. *Scientific Reports*, **9**(1), 1-7.
- ³⁶ Dahal, D., & Gumbs, G. (2017). Effect of energy band gap in graphene on negative refraction through the veselago lens and electron conductance. *Journal of Physics and Chemistry of Solids*, **100**, 83-91.
- ³⁷ Iurov, A., Gumbs, G., Roslyak, O., and Huang, D. (2013). Photon dressed electronic states in topological insulators: tunneling and conductance. *Journal of Physics: Condensed Matter*, **25**(13), 135502.
- ³⁸ Anwar, F., Iurov, A., Huang, D., Gumbs, G., & Sharma, A. (2020). Interplay between effects of barrier tilting and scatterers within a barrier on tunneling transport of Dirac electrons in graphene. *Physical Review B*, **101**(11), 115424.
- ³⁹ Iurov, A., Gumbs, G., Roslyak, O., and Huang, D. (2011). Anomalous photon-assisted tunneling in graphene. *Journal of Physics: Condensed Matter*, **24**(1), 015303.
- ⁴⁰ Mishra, K. A., & Kumar, U. (2019). Band Tuning of a Phosphorene Semiconductor via Floquet Theory. *Journal of Electronic Materials*, **48**(12), 8193-8205.
- ⁴¹ Iurov, A., Zhemchuzhna, L., Gumbs, G., and Huang, D. (2017). Exploring interacting Floquet states in black phosphorus: Anisotropy and bandgap laser tuning. *Journal of Applied Physics*, **122**(12), 124301.
- ⁴² Iorsh, I. V., Dini, K., Kibis, O. V., and Shelykh, I. A. (2017). Optically induced Lifshitz transition in bilayer graphene. *Physical Review B*, **96**(15), 155432.
- ⁴³ Gumbs, Godfrey and Huang, Danhong, *Properties of Interacting Low-Dimensional Systems*, (New York, John Wiley & Sons, Inc., June, 2011).
- ⁴⁴ Wunsch, B., Stauber, T., Sols, F., & Guinea, F. (2006). Dynamical polarization of graphene at finite doping. *New Journal*

- of Physics, **8**(12), 318.
- ⁴⁵ Hwang, E. H., & Sarma, S. D. (2007). Dielectric function, screening, and plasmons in two-dimensional graphene. *Physical Review B*, **75**(20), 205418.
 - ⁴⁶ Pyatkovskiy, P. K. (2008). Dynamical polarization, screening, and plasmons in gapped graphene. *Journal of Physics: Condensed Matter*, **21**(2), 025506.
 - ⁴⁷ Ezawa, M. (2012). Valley-polarized metals and quantum anomalous Hall effect in silicene. *Physical Review Letters*, **109**(5), 055502.
 - ⁴⁸ Tabert, C. J., & Nicol, E. J. (2014). Dynamical polarization function, plasmons, and screening in silicene and other buckled honeycomb lattices. *Physical Review B*, **89**(19), 195410.
 - ⁴⁹ Scholz, A., Stauber, T., & Schliemann, J. (2013). Plasmons and screening in a monolayer of MoS₂. *Physical Review B*, **88**(3), 035135.
 - ⁵⁰ Iurov, A., Gumbs, G., Huang, D., and Zhemchuzhna, L. (2017). Controlling plasmon modes and damping in buckled two-dimensional material open systems. *Journal of Applied Physics*, **121**(8), 084306.
 - ⁵¹ Sarma, S. D., & Li, Q. (2013). Intrinsic plasmons in two-dimensional Dirac materials. *Physical Review B*, **87**(23), 235418.
 - ⁵² Hwang, E. H., & Sarma, S. D. (2009). Screening-induced temperature-dependent transport in two-dimensional graphene. *Physical Review B*, **79**(16), 165404.
 - ⁵³ Iurov, A., Gumbs, G., and Huang, D. (2017). Temperature-dependent collective effects for silicene and germanene. *Journal of Physics: Condensed Matter*, **29**(13), 135602.
 - ⁵⁴ Iurov, A., Gumbs, G., Huang, D., and Balakrishnan, G. (2017). Thermal plasmons controlled by different thermal-convolution paths in tunable extrinsic Dirac structures. *Physical Review B*, **96**(24), 245403.
 - ⁵⁵ Patel, D. K., Ashraf, S. S., & Sharma, A. C. (2015). Finite temperature dynamical polarization and plasmons in gapped graphene. *Physica Status Solidi (b)*, **252**(8), 1817-1826.
 - ⁵⁶ Dadkhah, N., Vazifehshenas, T., Farmanbar, M., & Salavati-fard, T. (2019). A theoretical study of collective plasmonic excitations in double-layer silicene at finite temperature. *Journal of Applied Physics*, **125**(10), 104302.
 - ⁵⁷ Iurov, A., Gumbs, G., and Huang, D. (2018). Temperature-and frequency-dependent optical and transport conductivities in doped buckled honeycomb lattices. *Physical Review B*, **98**(7), 075414.
 - ⁵⁸ Gutierrez-Rubio, A., Stauber, T., & Guinea, F. (2013). Transverse current response of graphene at finite temperature: plasmons and absorption. *Journal of Optics*, **15**(11), 114005.
 - ⁵⁹ Iurov, A., Gumbs, G., & Huang, D. (2020). Thermal Collective Excitations in Novel Two-Dimensional Dirac-Cone Materials. *Nanoplasmonics*, (IntechOpen, London, 2020).
 - ⁶⁰ Dahal, D., Gumbs, G., & Huang, D. (2018). Effect of strain on plasmons, screening, and energy loss in graphene/substrate contacts. *Physical Review B*, **98**(4), 045427.
 - ⁶¹ Iurov, A., Gumbs, G., Huang, D., and Silkin, V. M. (2016). Plasmon dissipation in gapped graphene open systems at finite temperature. *Physical Review B*, **93**(3), 035404.
 - ⁶² Iurov, A., Huang, D., Gumbs, G., Pan, W., and Maradudin, A. A. (2017). Effects of optical polarization on hybridization of radiative and evanescent field modes. *Physical Review B*, **96**(8), 081408.
 - ⁶³ Andrade, E., Carrillo-Bastos, R., & Naumis, G. G. (2019). Valley engineering by strain in Kekule-distorted graphene. *Physical Review B*, **99**(3), 035411.
 - ⁶⁴ Iurov, A., Gumbs, G., Gao, B., and Huang, D. (2014). Modeling anisotropic plasmon excitations in self-assembled fullerenes. *Applied Physics Letters*, **104**(20), 203103.
 - ⁶⁵ Gumbs, G., Balassis, A., Iurov, A., and Fekete, P. (2014). Strongly localized image states of spherical graphitic particles. *The Scientific World Journal*, 2014.
 - ⁶⁶ Fessatidis, V., Horing, N. J., & Balassis, A. (2010). Power loss of an energetic charged particle moving parallel to a graphene sheet. *Physics Letters A*, **375**(2), 192-198.
 - ⁶⁷ Gusynin, V. P., & Sharapov, S. G. (2006). Transport of Dirac quasiparticles in graphene: Hall and optical conductivities. *Physical Review B*, **73**(24), 245411.
 - ⁶⁸ Sarma, S. D., & Madhukar, A. (1981). Collective modes of spatially separated, two-component, two-dimensional plasma in solids. *Physical Review B*, **23**(2), 805.
 - ⁶⁹ Gumbs, G., Iurov, A., Wu, J. Y., Lin, M. F., & Fekete, P. (2016). Plasmon excitations of multi-layer graphene on a conducting substrate. *Scientific Reports*, **6**, 21063.
 - ⁷⁰ Gumbs, G., Huang, D., & Talwar, D. N. (1996). Doublet structure in the absorption coefficient for tunneling-split intersubband transitions in double quantum wells. *Physical Review B*, **53**(23), 15436.
 - ⁷¹ Gumbs, G., & Huang, D. (2013). *Properties of Interacting Low-Dimensional Systems*. John Wiley & Sons.
 - ⁷² Huang, D., & Manasreh, M. O. (1996). Intersubband transitions in strained In_{0.07}Ga_{0.93}As/Al_{0.40}Ga_{0.60}As multiple quantum wells and their application to a two-colors photodetector. *Physical Review B*, **54**(8), 5620.
 - ⁷³ Huang, D., Rhodes, C., Alsing, P. M., and Cardimona, D. A. (2006). Effects of longitudinal field on transmitted near field in doped semi-infinite semiconductors with a surface conducting sheet. *Journal of Applied Physics*, **100**(11), 113711.
 - ⁷⁴ There was a typographical error in Ref. ¹⁷ where this Hamiltonian was first derived.